Strategies to overcome photobleaching in algorithm-based adaptive optics for nonlinear *in-vivo* imaging

M. Caroline Müllenbroich
Ewan J. McGhee
Amanda J. Wright
Kurt I. Anderson
Keith Mathieson

Strategies to overcome photobleaching in algorithm-based adaptive optics for nonlinear *in-vivo* imaging

M. Caroline Müllenbroich,a Ewan J. McGhee,b Amanda J. Wright,c Kurt I. Anderson,b,*,† and Keith Mathiesona,†
aUniversity of Strathclyde, Scottish University Physics Alliance, Institute of Photonics, Wolfson Centre, 106 Rottenrow, G4 0NW Glasgow, United Kingdom
bBeatson Institute for Cancer Research, Switchback Road, Bearsden, G61 1BD Glasgow, United Kingdom
cUniversity of Nottingham, Institute of Biophysics, Imaging and Optical Science, University Park, Nottingham NG7 2RD, United Kingdom

Abstract. We have developed a nonlinear adaptive optics microscope utilizing a deformable membrane mirror (DMM) and demonstrated its use in compensating for system- and sample-induced aberrations. The optimum shape of the DMM was determined with a random search algorithm optimizing on either two photon fluorescence or second harmonic signals as merit factors. We present here several strategies to overcome photobleaching issues associated with lengthy optimization routines by adapting the search algorithm and the experimental methodology. Optimizations were performed on extrinsic fluorescent dyes, fluorescent beads loaded into organotypic tissue cultures and the intrinsic second harmonic signal of these cultures. We validate the approach of using these preoptimized mirror shapes to compile a robust look-up table that can be applied for imaging over several days and through a variety of tissues. In this way, the photon exposure to the fluorescent cells under investigation is limited to imaging. Using our look-up table approach, we show signal intensity improvement factors ranging from 1.7 to 4.1 in organotypic tissue cultures and freshly excised mouse tissue. Imaging zebrafish *in vivo*, we demonstrate signal improvement by a factor of 2. This methodology is easily reproducible and could be applied to many photon starved experiments, for example fluorescent life time imaging, or when photobleaching is a concern. © *2014 Society of Photo-Optical Instrumentation Engineers (SPIE)* [DOI: 10.1117/1.JBO.19.1.016021]

Keywords: adaptive optics; aberrations; fluorescence; microscopy; photobleaching.

Paper 130612PRR received Aug. 21, 2013; revised manuscript received Dec. 11, 2013; accepted for publication Dec. 13, 2013; published online Jan. 27, 2014.

1 Introduction

Two photon excitation fluorescence (TPEF) microscopy[1] is capable of imaging biological tissue noninvasively with submicrometer resolution and is often the method of choice for investigating cells and cellular functions in deep tissue imaging. It has application to a variety of fields including neuroscience, immunology, and cancer research.[2] In an attempt to image ever deeper into biological tissues, nonlinear microscopy has moved toward infrared wavelengths. Infrared nonlinear microscopy enables the use of red fluorophores and proteins, doubles imaging depth, and strongly reduces phototoxicity and photobleaching compared with conventional nonlinear microscopy.[3] However, a central limitation of imaging remains—scattering and distortion of the beam profile through optical aberrations. Aberrations introduced either by the system's optical setup or the sample under investigation cause an elongation and broadening of the diffraction limited focal spot, shown to severely degrade nonlinear microscopy.[4–6] In nonlinear microscopy, an aberrated focal spot not only results in decreased resolution but also a considerable loss of signal intensity as signal scales with the square of laser intensity.[7] The amount of aberrations introduced by a sample can be manipulated in various ways. Adaptive optics (AO)[8] provides a means to compensate for optical aberrations and is capable of restoring resolution and signal strength when imaging at depth, thus allowing for deeper tissue imaging.[9,10] The principle of the AO involves generating a preshaped wavefront with equal but opposite distortion to that which degrades image quality by means of an active element, for example a spatial light modulator or deformable membrane mirror (DMM).

Several research groups have investigated the benefits of adaptive wavefront correction in nonlinear microscopy either by closing the loop with a wavefront sensor or in wavefront sensorless schemes by using optimization algorithms. The first implementation of adaptive aberration correction in TPEF microscopy was reported by Neil et al.[11] They used a spatial light modulator to measure the specimen-induced aberrations and apply the phase conjugate of these aberrations to the imaging laser beam. Rueckel et al.[12] used a closed-loop adaptive wavefront correction based on sensing the wavefront of coherence gated backscattered light, to substantially improve imaging in living biological samples. The confocal principle for depth selection was chosen by Cha et al.[13] to detect reflected light from the focal region of a multiphoton microscope and measure its wavefront distortion. In a new development, fluorescent light, emitted by artificial guide stars, has been used to measure the aberrations with a wavefront sensor in order to apply the optically conjugated aberrations with a DMM. The reference sources employed were either injected fluorescent microspheres or nonlinear guide stars created by the TPEF.[14–16] A drawback of those closed loop methods is the loss of power due to the

continuous monitoring of the wavefront and/or use of a spatial light modulator as well as the complexity of the setup. Additionally, measuring distorted wavefronts in microscopy is not trivial and generally requires a point source emitter in the sample. In wavefront sensorless applications, fluorescence signal strength is often optimized by varying the shape of the incoming light via genetic algorithms,[17–20] or image-based algorithms,[21–23] although other feedback parameters like contrast and resolution have also been investigated.[24] Using a search algorithm in conjunction with a merit factor has the distinctive advantage of eliminating the need for re-imaging and wavefront sensing, thus reducing complexity and cost of the system.

Optimization algorithm approaches, however, often involve exposing a small region of interest (RoI) to continuous laser light for tens of minutes while the algorithm converges, making this region liable to photobleaching. This situation is aggravated in nonlinear microscopy, where two-photon excitation bears an inherent trade-off between low off-focus and severe in-focus photobleaching.[25] Photobleaching, the permanent destruction of fluorophores, and photodamage, the photodynamic damage to the tissue mediated by fluorophores, are both common problems in fluorescence microscopy[26] and often a limiting factor for the imaging of live tissue. For live cell microscopy, repeated exposure to laser light leads to photobleaching of fluorophores associated with *de novo* formation of reactive oxygen intermediates, ultimately compromising imaging sensitivity as well as cell viability and function.[25] The key motivation of this work is to overcome photobleaching and photodamage associated with optimization algorithm-based AO in nonlinear microscopy using a variety of techniques. We use a DMM as the corrective element in conjunction with a random search optimization algorithm that rapidly alters the DMM shape until a merit factor, either TPEF or second harmonic generation (SHG) signal intensity, is satisfactorily improved.

We demonstrate several strategies to overcome photobleaching and photodamage. Concerning the general random search algorithm, we implemented three major adaptations: a dedicated bleaching compensation routine, a Gaussian weighted random selection process, and the use of preoptimized DMM shapes as intelligent starting points for new optimizations. These approaches speed up the optimization routine and further reduce the effect of photobleaching. The other main aspect of our approach is to apply the optimization routine on a variety of test samples to generate a look-up table of preoptimized DMM shapes, including using a second harmonic signal that does not suffer from photobleaching to create a look-up table of shapes that can then be applied to a multiphoton image. In this way, the exposure of the target sample to photons is minimized to the imaging. In the work presented here, we demonstrate the use of the above listed techniques for signal enhancement in three different signal sources: a fluorescent solution of erythrosine (Sec. 3.1), fluorescent beads which were loaded into tissue cultures during maturation (Sec. 3.2) and on intrinsic SHG signal, which does not suffer from photobleaching (Sec. 3.3). Whereas optimizing on the TPEF signal of a fluorescent dye corrects mainly for system-induced aberrations, the optimization on randomly distributed beads within tissue cultures results in depth specific optimizations. We investigate the robustness of the look-up table over time and demonstrate that optimizations performed on the SHG increase the TPEF intensity and *vice versa*. The wavefront compensation for system- and sample-induced aberrations in organotypic

tissue cultures and freshly excised mouse tissue result in signal intensity improvement factors ranging from 1.7 to 4.1. Finally, in Sec. 3.4, we validate our methodology with the *in vivo* imaging of zebrafish. A DMM shape from the look-up table acquired 3-days prior to the imaging results in an immediate signal improvement by a factor of 2. Increasing the signal-to-noise ratio at depth allows for the incident laser power to be reduced, which decreases the risk of photobleaching and improves sample viability. To name just one application, our approach will be highly useful in cancer cell invasion studies where an organotypic tissue matrix is imaged 1 day after the cancer cells have been deposited on top of the matrix and then over the next 21 days (or longer) to assess biological processes, such as invasion, proliferation, survival, or differentiation.[27]

2 Experimentation

2.1 *Experimental Setup*

The experimental setup combines nonlinear imaging within an inverted microscope (Nikon Eclipse, Kingston upon Thames, UK, TE2000-U,) and an AO system for aberration correction. A Ti:Sapphire femtosecond-pulsed laser (Chameleon, Coherent UK) with a repetition rate of 80 MHz, was used to pump an optical parametric oscillator (OPO) (MIRA, Coherent Ape, Ely, UK), which was tuned to emit at the wavelength of 1098 nm. The OPO reduces photobleaching and scattering in the infrared wavelengths.[28–30] The OPO beam is directed toward the active region of the DMM with an incident angle of 0 deg by using appropriate polarization optics (Fig. 1). The DMM employed in this work (Mini-DM, Boston Micromachines Corporation, Cambridge, Massachusetts) uses 32 independent electrostatic actuators to control the shape of the highly reflective, gold-coated membrane. The DMM is re-imaged onto the closed-coupled galvanometer scan mirrors inside a commercial scanhead (Trim-scope, LaVision BioTec, Bielefeld, Germany). All imaging was performed with a 100× 1.3 NA oil immersion objective (Nikon), which focuses the light into a sample mounted on an *xyz* translation stage. Scanning and image acquisition was done with the commercial software of LaVision BioTec, (Bielefeld, Germany). The blue-shifted fluorescence is detected by nondescanned detector photomultiplier tubes (PMTs, Hamamatsu H6780-20-LV 1M) located at the back focal plane of the objective. A combination of a dichroic mirror (Semrock, Rochester, New York, DIOR594 LP) and two emission filters (SHG: Semrock 549/15 BP, TPEF: Semrock 630/60 BP) allows for the simultaneous detection of SHG and TPEF in two detection channels. In the following, the PMT with the SHG filter will be referred to as the green channel and the PMT with the TPEF filter as the red channel. The modal content of the DMM shapes was determined by Zernike mode decomposition measured by replacing the microscope objective with a Shack-Hartmann wavefront sensor (Thorlabs, Newtown, New Jersey, WFS150C). The focusing geometry in the inverted microscope is schematically depicted in Fig. 1(b) and serves to define system- and sample-induced aberrations. Here, system-induced aberrations encompass all aberrations that occur when focusing the laser through the immersion oil and the coverslip onto the surface of the sample. This minimum geometry is required as our approach necessitates the laser to come to focus to create an optimization probe. Aberrations that occur because the focal spot is moved deeper into the sample, we termed
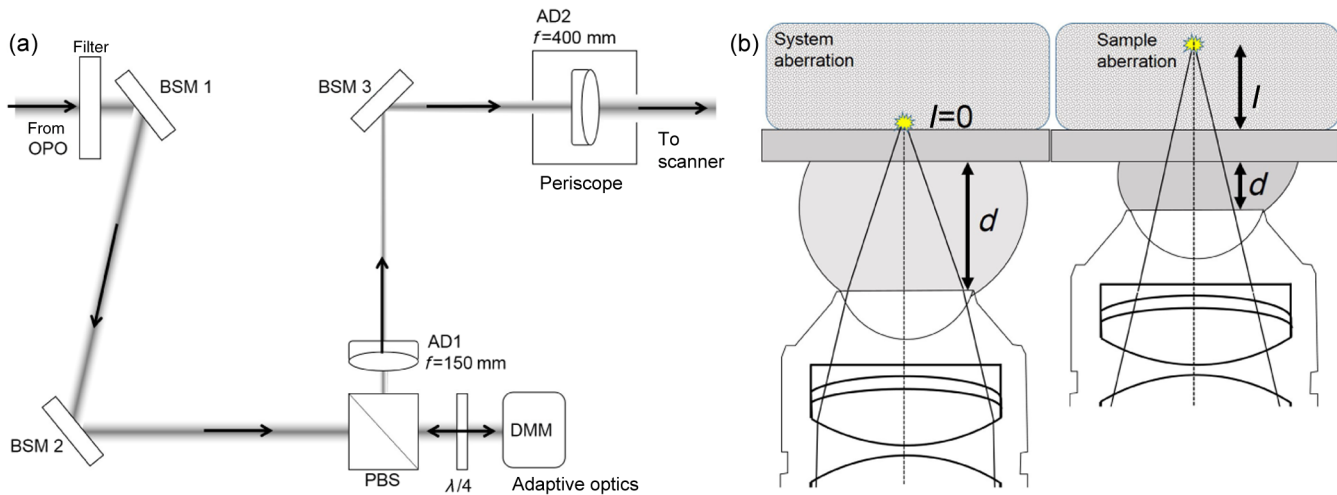
Fig. 1 (a) Adaptive optics components. OPO: optical parametric oscillator, BSM1-3: beam steering mirrors, AD: achromatic doublets, PBS: polarising beam splitter cube, $\lambda/4$: quarter-wave plate, DMM: deformable membrane mirror. (b) Schematic defining system and sample induced aberrations.

sample induced. The latter include changes in the distance d between the tip of the microscope objective and the coverslip, the distance l which corresponds to the imaging depth within the sample and any aberrations arising from the local variations in refractive index within the sample itself.

2.2 Random Search Algorithm and Bleaching Compensation

The aberration correction required was determined in a wavefront sensorless approach by rapidly altering the mirror shape with a random search algorithm using the TPEF or the SHG signal intensity as a merit factor. Random search algorithms have the advantage over more elaborate algorithms, such as genetic ones, of using less parameters and variables, and yielding high enhancement factors in reasonable lengths of time. Additionally, random search algorithms are able to localize global extrema rather than local extrema as opposed to simpler algorithm such as hill climbing.[31] The random search algorithm used in this work was implemented in LabVIEW and has previously been successfully applied to the AO in optical trapping, confocal microscopy, and coherent anti-Stokes Raman scattering.[32,33]

In order to be able to optimize on a signal that will intrinsically decline with time due to photobleaching, a dedicated bleaching compensation routine (Fig. 2) was programmed into the general random search algorithm.[34] With this compensation, the merit factor is continually renormalized to a revised lower value to account for photobleaching. The optimizations were performed on three different sources for the merit factor; first, a solution of the fluorescent dye erythrosine, second, on fluorescent beads which were loaded into the tissue cultures during maturation, and third on the SHG signal intrinsic to the tissue cultures that does not suffer from photobleaching. Optimizations were stopped by the user after at least 100 successful iterations which meant that, on average, each actuator had been changed approximately three times. After the optimization procedure, an image was immediately acquired with the optimized and the unoptimized DMM, respectively. Due to the random nature of the algorithm, optimizations can take up a considerable amount of time (≈ 30 min) and therefore make *in situ* optimizations for each given depth impractical. Instead,

it has been proposed to use look-up tables, which consist of preoptimized DMM shapes that can be called upon for imaging at certain depths.[33] An incremental approach allowed the use of a previously optimized DMM shape from a shallower depth as an intelligent starting point for the optimization at hand to reduce convergence time.[35] Additionally, the actuator selection process was weighted with a Gaussian function to preferentially select the central actuators, which have a greater influence on the overall DMM shape than those in the periphery. Both approaches sped up the optimization process, meaning the sample is exposed to less photons, and the effect of photobleaching is further reduced.

2.3 Samples

Three biologically relevant tissues were investigated in this work. First, Lifeact mouse[36] tissue was used to analyse the correction of system-induced aberrations. The Lifeact mouse expressed the Tag-RFPtp, which labels actin filaments, a central component of muscle fibers and the cytoskeleton. Mice were sacrificed immediately prior to imaging, and skin and gut tissue were excised and placed in phosphate buffered saline. Muscle relaxant (scopolamine) was added to the gut to avoid peristaltic movement. Second, organotypic collagen I assays were used to test the depth specificity and time robustness of the optimized DMM shapes. Organotypics are important intermediate tissue culture systems often replacing living animal samples. The cultures are composed of primary fibroblast cells, acquired from a human forearm, and type I collagen, extracted from the tendons of rat tails. The organotypic cultures used in this work have all been grown in house at the Beatson Institute of Cancer Research and a detailed protocol for their production can be found in Timpson et al.[27] The fibroblast cells contract the gel-like collagen so that it assumes fibrillar form. The fibrillar collagen exhibits narrow band SHG with a maximum at 1100 nm from a broad input wavelength range[3] whereas the living fibroblast cells are transfected with mCherry and can be imaged via TPEF. Fluorescent beads of 4-μm diameter (T7283 tetraspeck, Invitrogen, Paisley, UK) were loaded into the organotypics before contraction and became randomly distributed through the tissue. The beads are stained throughout with four different fluorescent dyes and therefore appear in both the green and
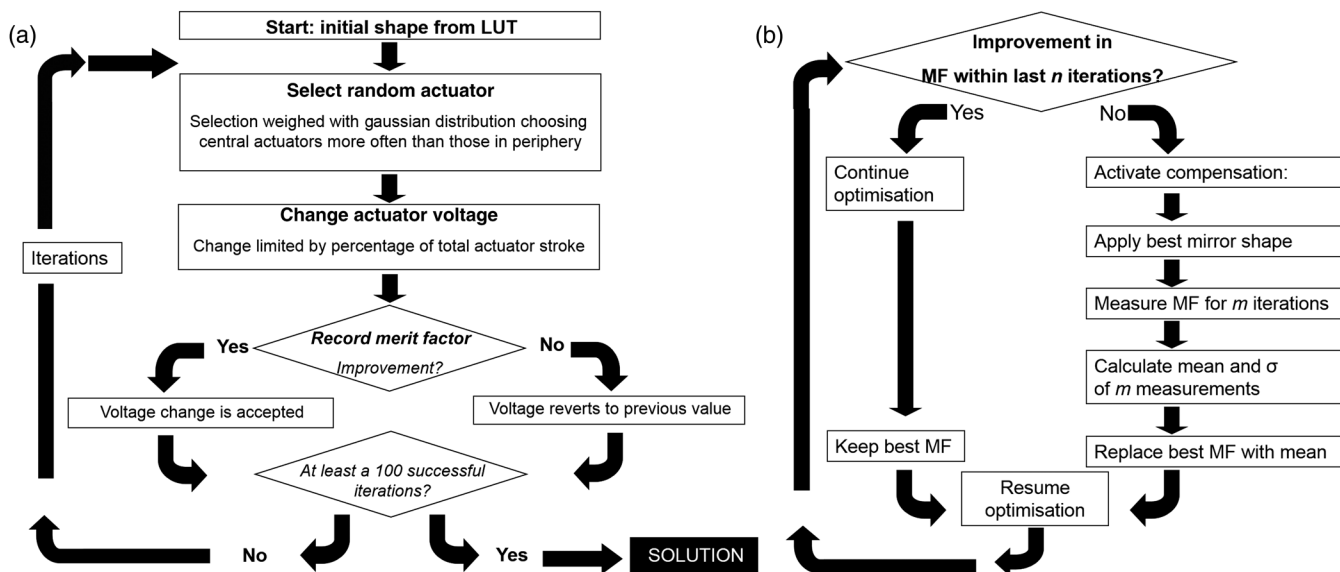
Fig. 2 (a) Random search algorithm flow chart depicting one iteration. (b) Bleaching compensation loop. MF: merit factor, σ: standard deviation.

the red channels, albeit with varying intensities. The fluorescent beads as well as the intrinsic SHG signal were used as a source for the merit factor to perform optimizations at depth within tissue. Third, a transgenetic zebrafish embryo was imaged *in vivo* to validate the look-up table methodology. The fish embryo was 3.5 days postfertilisation and mounted live in agarose gel on a coverslip. The fish was anaesthetised with tricaine mesylate dissolved in water. The fish exhibited green fluorescent protein (GFP)-labelled wt1b protein in developing kidney tissue and mCherry-labelled Flk1 protein in developing vasculature.

3 Results

3.1 Optimizations on Fluorescent Dye

An aqueous solution of erythrosine with a refractive index of 1.33 was added to a 50:50 mix of sucrose with phosphate-buffered saline such that a fluorescent solution with a refractive index of 1.39, close to that of many biological tissues,[37] was obtained. The solution is effectively free from photobleaching because bleached dye molecules diffuse out of the focal volume. This solution was used to run an optimization on the TPEF signal at a depth of 10 μm. The obtained DMM shape, corrected presumably for system aberrations, was used to image *ex vivo* Lifeact mouse tissue in which Lifeact binds to filamentous actin. Figure 3 shows images of the collagen (green channel, SHG) and vasculature (red channel, TPEF) in mouse skin obtained with the unoptimized DMM shape (a) and with the DMM shape optimized on the fluorescent signal of the erythrosine (b). The evolution with depth of the SHG signal within a small, central RoI (c) was used to calculate the improvement factors (d). The average signal improvement through the depth of the stack was 1.9 ± 0.2 in the SHG channel. The freshly excised Lifeact mouse intestine was imaged in a stack of 60-μm depth, however, the beginning of the stack did not coincide with the surface of the tissue but with the onset of the smooth muscles. The start of the stack was $\approx$70-μm deep in the tissue. Figures 3(e)–3(l) compare the unoptimized with

the optimized images at increasing depths of 15, 24, and 37 μm. The TPEF intensity in a small central RoI is shown in Fig. 3(m) and the improvement factors calculated from that data are shown in Fig. 3(n). On average through the entire depth of the stack, the signal was improved by a factor of 1.7 ± 0.2. The improvement factor was slightly lower than in the case of the mouse skin because the stack was taken $\approx$70-μm deeper within the tissue.

3.2 Optimizations on Fluorescent Beads Embedded in Organotypic Tissue Cultures

3.2.1 Depth specificity of optimizations

In the previous section, the optimization on a fluorescent solution gave a DMM shape that corrected mainly for system induced aberrations. In this section, optimized DMM shapes that have been acquired at specific depths within tissue are investigated. An organotypic tissue culture loaded with randomly distributed fluorescent beads of 4-μm diameter during maturation provided a test sample to acquire a depth specific look-up table. At first, the TPEF signal of a bead at a depth of 15 μm was used as a merit factor to perform an optimization. This DMM shape was saved as the first entry in the look-up table and then used as the starting point for an optimization on the TPEF signal of a bead at a depth of 38 μm. This shape was saved as a second entry in the look-up table and used as the starting DMM shape for the optimization on the TPEF signal of a third and last bead at a depth of 144 μm. In this way, a look-up table was created which contained three preoptimized DMM shapes for these three depths plus the unoptimized DMM shape. Using these four DMM shapes, four stacks of the same piece of organotypic tissue were recorded. The stacks had a total depth of 160 μm acquired in 3-μm steps. Figure 4(a) shows the axial intensity profiles of the three beads for each DMM shape. The degradation in intensity due to an increase in imaging depth of 129 μm from 15 to 144 μm can be seen in the reduction of the signal obtained with the unoptimized DMM shape (black squares) by roughly 50%.
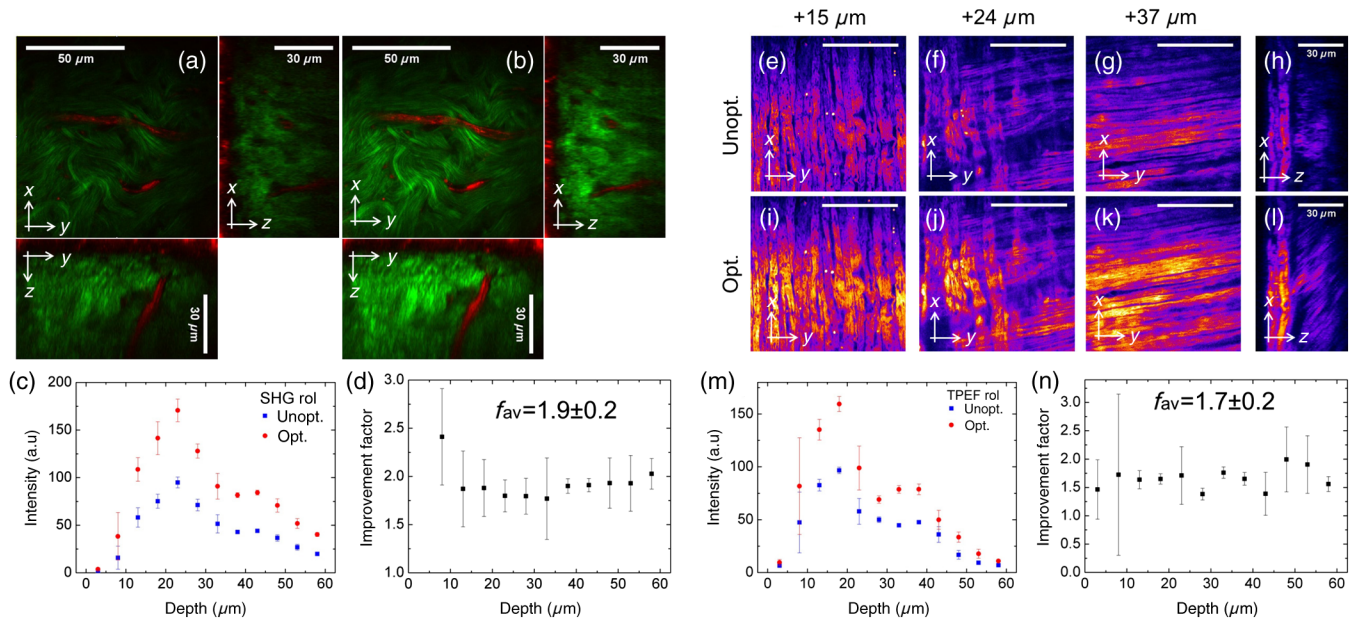
Fig. 3 *Ex-vivo* Lifeact mouse skin imaged at a depth of 30 μm (a) without and (b) with aberration correction. Green channel: SHG emitted by collagen; Red channel: TPEF emitted by vasculature. (c) SHG signal within a central RoI with depth. The data was binned over 5 μm to display an average signal intensity and error bars given by a standard deviation. (d) Calculated signal improvement factors. (e to l) Lifeact mouse intestine showing orthogonally oriented layers of smooth muscle imaged without and with aberration correction. The first slice of the stack lay $\approx$70-μm deep within the tissue. The three depths presented were measured with respect to the start of the image stack. Scale bar: 50 μm, false colour scale applied for clarity. (m) TPEF signal (red channel) within a small, central RoI with depth, and (n) calculated signal improvement factors.

The depth specificity of the optimizations also becomes apparent: for the beads at 15- and 38-μm depths, the shallow optimizations (blue circles, green triangles) led to the highest signal improvements whereas for the bead at 144 μm the optimization performed at 144 μm (red triangles) resulted in the highest signal improvement. This gave an indication as to the required "step size" in depth in which optimizations are ideally acquired to generate the highest intensity signals with the least amount of entries in the look-up table. Optimizations which were 30 to 50-μm apart along the optical axis perform similarly, and therefore we estimated that optimizations are only required every 50 μm for this sample. The signal improvement factors were calculated as the amplitude of the fitted Gaussian function after optimization divided by the amplitude obtained with the unoptimized DMM shape. The optimization performed at 144 μm led to a 1.7-fold improvement at all three depths, whereas both shallow optimizations showed a higher peak improvement by 3-fold at the shallow depths while actually decreasing the signal of the bead embedded within the organotypic at a depth of 144 μm. In Figs. 4(b) and 4(c), the fluorescent bead that was used as a guide star for the optimization at a depth of 144 μm and neighboring fibroblast cells are shown with and without aberration correction. In Fig. 4(d), the lateral intensity profile through the indicated RoI revealed an improvement in signal intensity of the fluorescent cells by roughly 2.5-fold at a depth of 147 μm.

3.2.2 *Robustness of the look-up table with time*

Three days later, two new optimizations on the TPEF signal of fluorescent beads embedded in the same organotypic tissue culture at depths of 11 and 98 μm were added to the look-up table and compared with the previously acquired optimizations at depths of 38 and 144 μm. The shape optimized at a depth of 15 μm was omitted due to its similarity with the shape optimized at 38 μm. In this way, the variation of applicability of the optimizations with time was tested: optimizations acquired 3 days before imaging were compared with optimizations acquired immediately prior to the imaging. The comparison was made by acquiring five stacks, spanning a depth of 112 μm in 1-μm steps, one with each shape in the look-up table as well as the unoptimized DMM shape. It should be noted that the organotypic tissue cultures keep contracting with time and this leads to a slight variation in tissue density.

Figure 5 shows the axial intensity profiles of the multidye-stained beads at depths of 11 and 98 μm acquired with each DMM shape of the look-up table in the red and green channels. The optimization performed on the same day at the exact depth led to the highest signal improvement by an average of 2.1-fold for both beads in both channels. The optimization performed 3 days previously at a similar depth, i.e., within the previously discussed step size along the optical axis, led to a slightly reduced overall signal improvement. On average for both beads in both channels the signal was improved by a factor of 1.7. Table 1 lists each value for each case. The shapes in the look-up table performed as expected with the trend of decreasing improvement in signal intensity with distance between depth of imaging/optimization acquisition and time between optimization/imaging. The relative signal improvement was higher in the green channel compared to the red channel because the signal was two orders of magnitude weaker, and therefore any improvement in the shape of the wavefront led more readily to drastic changes in signal generation.
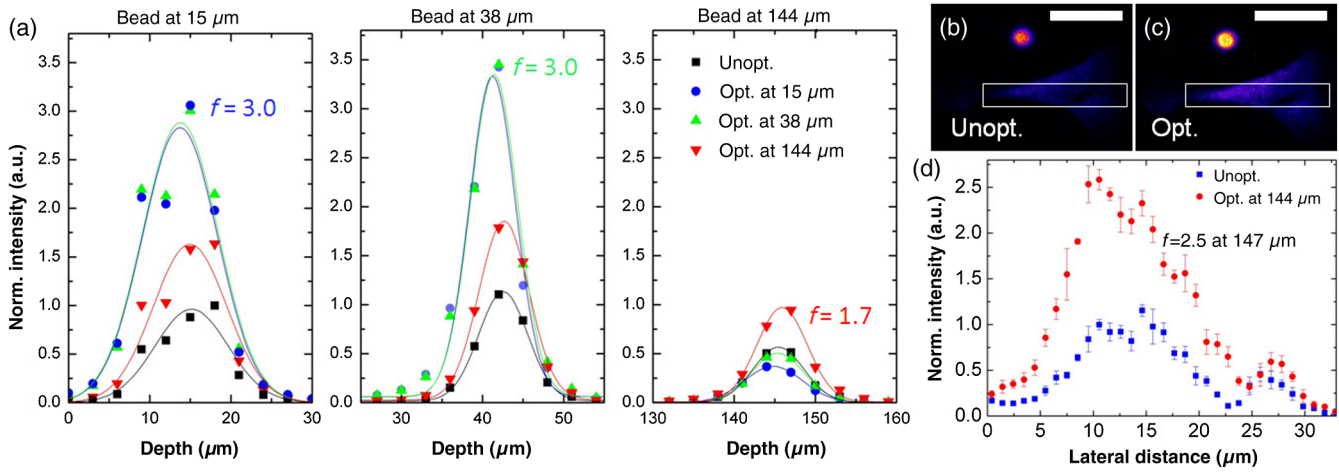
Fig. 4 (a) Axial intensity profiles through beads at the depths of 15, 38, and 144 μm embedded within the organotypic tissue culture. (b to c) Detail showing the bead and adjacent cells at a depth of 144 μm without and with correction in the red channel (false colour scale applied for clarity). Scale bar: 15 μm. (d) Lateral intensity profile (binned over 1 μm, error bars: one standard deviation) within the indicated RoI.
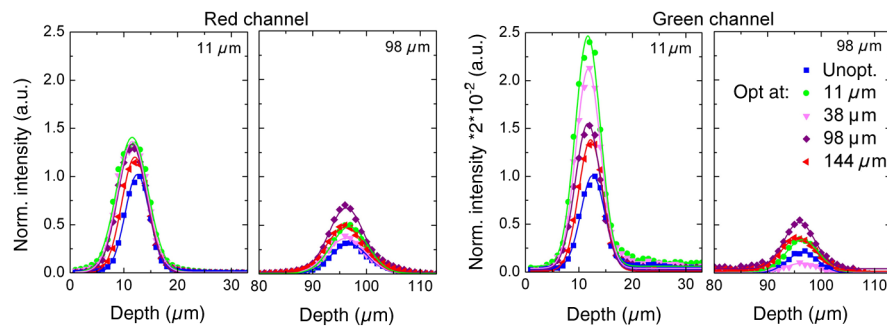

Fig. 5 Axial intensity profiles of multiply dye-stained beads at depths of 11 and 98 μm with all DMM shapes in the look-up table for the red and green channel. The intensity in each channel was normalised to unity for the unoptimized DMM shape for the bead at the shallowest depth of 11 μm. The intensity in the green channel was scaled to the intensity in the red channel by renormalisation of the y-axis. Table 1 lists the amplitude of the Gaussian fits A to the intensity profiles and the calculated improvement factors f. The first column indicates the time difference Δ in days between the acquisition of the optimization and the image.

Table 1 Amplitude of the Gaussian fits A to intensity profiles and calculated improvement factors f.

		Red channel			Green channel		
		shallow-(11 μm)	deep bead (98 μm)		shallow-(11 μm)	deep bead (98 μm)	
Δ [d]	LUT	A	A	f	A	A	f
—	Unopt.	1.00	0.31	—	1.00	0.21	—
0	11 μm	1.40	0.48	1.55	2.41	0.34	1.62
3	38 μm	1.36	0.37	1.19	2.08	0.45	0.43
0	98 μm	1.34	0.67	2.16	1.53	0.48	2.29
3	144 μm	1.20	0.48	1.55	1.37	0.35	1.67

3.3 Optimizations on SHG Generated in Organotypic Tissue Cultures

In the previous sections, optimizations were performed on the TPEF signal of fluorescent dye and beads. The intrinsic decrease of fluorescence intensity over time due to photobleaching was compensated with a re-normalization loop in the random search algorithm. The organotypic tissue cultures used in this work are partly composed of collagen and therefore allow for the possibility of optimizing on an intrinsic SHG signal. This SHG signal provides for an optimization procedure that is not limited by photobleaching while reducing photoexposure to fluorescent structures of interest. An intrinsic SHG signal has the additional advantage over fluorescent beads that the bright signal from the latter can pollute the fluorescent image and hide small sample features. The SHG, like TPEF, is a second-order nonlinear process, and therefore the SHG shows the same nonlinear sensitivity to the focal volume as TPEF. In order to determine the sensitivity of the optimization procedure to the signal source of the merit factor a comparison was drawn between three DMM shapes. The first shape was acquired by optimizing on the intrinsic SHG signal generated within a small RoI at a depth of 19 μm within an organotypic tissue culture. The second DMM shape was the previously discussed shape from the look-up table that was optimized on the TPEF signal of a bead embedded at a depth of 98 μm and the third and last shape was the unoptimized DMM shape. All three DMM shapes were applied to the imaging of organotypic tissue cultures in the TPEF and the SHG modality by acquiring three stacks with a depth of 112 μm and a step size of 1 μm. Figures 6(a)–6(c) compare images at a depth of 11 μm acquired with the three DMM shapes, and Figs. 6(d)–6(f) show the performance of the same DMM shapes at a depth of 98 μm within the organotypic tissue. Figures 6(g) and 6(h) show the axial intensity profiles of the beads in both channels. Irrespective of the signal source used for the optimization, the signal improvement was highest in the images acquired with the DMM shape, which was optimized and close to the imaging depth. Figures 6(i) and 6(j)

compare the modal content of each DMM shape of the look-up table discussed so far in terms of their higher order Zernike coefficients. The coefficients that were measured with the shape optimized at the shallowest depth (11 μm) in the look-up table were subtracted to obtain changes solely due to depth dependency. The dominant higher-order aberrations were trefoil and tetrafoil. Whereas some aberrations like coma in y remain fairly constant, which implies that they are predominantly system induced. Other aberrations, like spherical aberration and secondary astigmatism in y, show a distinctive trend with depth and this was taken as indication that their origin was due to the sample.

Figure 7 quantifies the signal improvement by the same DMM shape optimized on the SHG compared to the unoptimized DMM shape for both imaging modalities. In Figs. 7(a) and 7(b), the SHG signal emitted by the collagen (green channel), and in Figs. 7(c) and 7(d), the fluorescent fibroblast cells (red channel) are shown. The intensity profile with depth within a small, central RoI in the SHG channel, Fig. 7(e) was used to calculate the development of the improvement factor with depth [Fig. 7(f)]. The signal improvement factor increased with depth and reached a peak value of 4.1 ± 0.6 at a depth of 111 μm. The average signal improvement through the entire range of depth of 112 μm was 2.5 ± 0.5. In the TPEF channel, such a development of improvement factor with depth was not easily obtained due to the inhomogeneous distribution of the fibroblast cells throughout the organotypic tissue culture. Instead, several RoIs were used at various lateral positions throughout the depth of the stack coinciding with the occurrence of fibroblast cells. An exemplary axial intensity profile of a cell, Fig. 7(g) yielded a signal improvement for the TPEF channel of 3.5-fold at a depth of 106 μm. Figure 7(h) shows the accumulation of four cell fluorescence intensity profiles at various depths. Averaging six cells with depths ranging from 14 to 106 μm, the improvement factor was 2.8 ± 1.1. The large variance is caused by varying staining levels, cell sizes, and different lateral positions leading due to an inhomogeneous distribution of fluorophores.
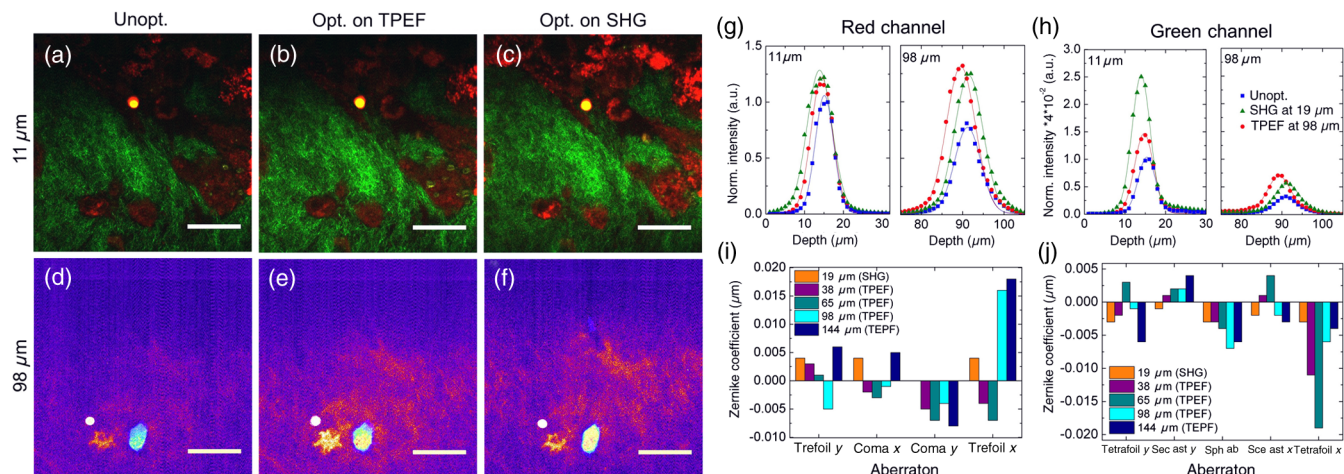

Fig. 6 Organotypic tissue culture at a depth of 12 μm (a to c) and at a depth of 98 μm (d to f) (false colour scale applied for clarity). Red channel: TPEF emitted by fibroblast cells; green channel: SHG emitted by collagen. The scale bar is 25 μm. Axial intensity profile of beads at depths of 11 and 98 μm in the red channel, (g) and in the green channel (h). The beads were imaged with the DMM shape pre-optimized on SHG at a depth of 19 μm, the DMM shape preoptimized on TPEF signal of a bead at a depth of 98 μm and the unoptimized shape. (i,j) Zernike coefficients for the Zernike aberrations of the third and fourth order.
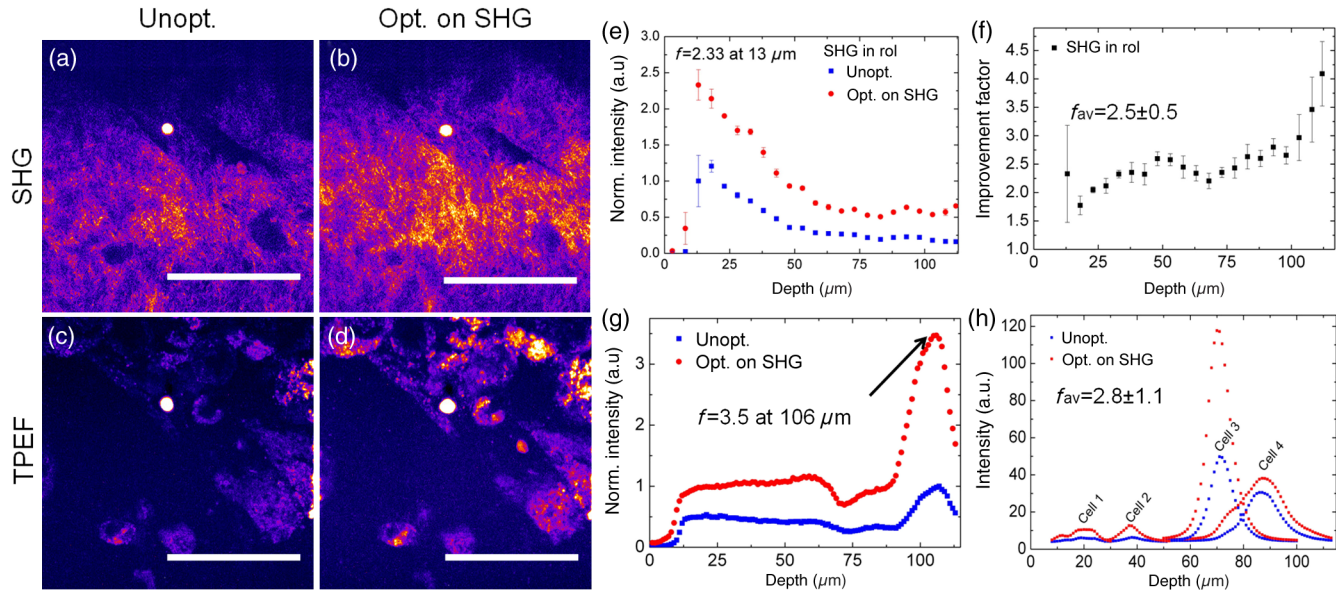
Fig. 7 (a,b) SHG emitting collagen and (c,d) TPEF emitting fibroblast cells at a depth of 11 μm within an organotypic tissue in false colour scale. (e) SHG signal development with depth within a small, central RoI (not shown for clarity). The SHG signal was binned over a depth of 5 μm to yield average signal with the error bars representing one standard deviation. (f) Improvement factors calculated from (e). The average improvement factor was calculated over the entire range of depths. (g) The TPEF signal of a fibroblast cell within a small RoI. (h) Accumulation of four cells at various lateral and axial positions. The average improvement factor was calculated with six cells throughout the depth of the stack.

3.4 In Vivo Imaging of Zebrafish

To validate the look-up table methodology, *in vivo* imaging of zebrafish was performed. Zebrafish are important animal models for the study of morphogenesis,[38] cardiac development,[39] and human disease[40] to name just a few and are particularly suited for optical imaging due to the relative transparency of the embryo.[41] The DMM shape chosen from the look-up table for the imaging was preoptimized on the TPEF signal of a fluorescent bead embedded at a depth of 144 μm in an organotypic tissue culture 3 days prior to the imaging. Figures 8(a) and 8(b) show images obtained at a depth of 69 μm with and without aberration correction. The developing kidney tissue (green channel) was excited with the Ti:Sapphire laser and does not profit from aberration correction because the DMM is not in the optical path. The developing vasculature (red channel) was excited with the OPO and is affected by the shape on the DMM. Figures 8(c) and 8(d) show details at a depth of 100 μm. The axial signal intensity development is shown in Fig. 8(h) where the pixel brightness within the indicated RoI is shown after subtraction of a common background value for both channels. Averaging over the last 30 μm of the stack, the signal was improved by a factor of 1.9 ± 0.3. Figures 8(e) and 8(f) show vasculature at a depth of 54 μm and the RoI considered in Fig. 8(g). The axial intensity profile
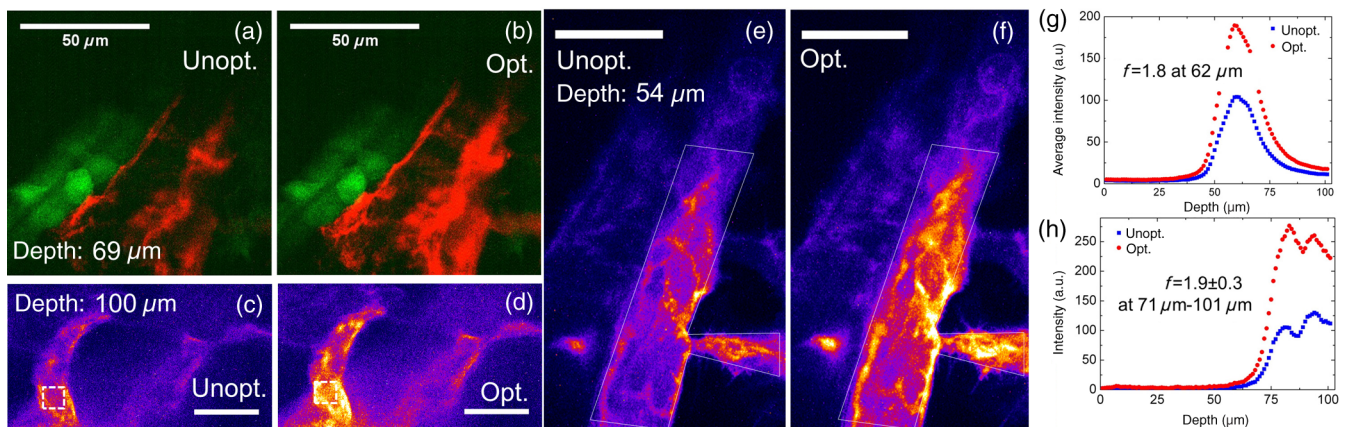

Fig. 8 *In vivo* imaging of anaesthetised zebrafish (a) with the unoptimized shape and (b) with a shape from the look-up table. The DMM shape was preoptimized on a fluorescent bead embedded in organotypic tissue at a depth of 144 μm 3-days prior to the imaging. Green channel: Ti:Sa excited TPEF of kidney tissue; red channel: OPO excited TPEF of vasculature.

yields an improvement by 1.8-fold at a depth of 62 μm. These levels of improvement are consistent with levels expected for the correction of system aberrations according to Sec. 3.1.

4 Discussion

Our method of using algorithm-generated DMM shapes from a look-up table offers two distinct advantages. The first is that the hardware demands are minimal as no additional optical elements for wavefront measurement are required. All of the essential mechanism for wavefront correction is contained in the optimization algorithm and therefore encapsulated in LabVIEW code. Second, once a basic look-up table for a stable setup has been acquired, a significant increase in signal intensity can be achieved instantly and over several days by applying these preoptimized DMM shapes. The level of improvement in signal intensity achieved in this study compares well with previously published data and is generally higher.[13,14,19,22,23,42,43] In this work, using the look-up table approach, the signal intensity was improved, on average up to a depth of 112 μm within organotypic tissue cultures, by a factor of 2.5 ± 0.5 for SHG and 2.8 ± 1.1 for TPEF with peak values of up to 4.1 ± 0.6. The same shapes were used to increase the quality of *in vivo* images in zebrafish three days after the DMM shapes had been acquired. The immediate signal improvements observed while imaging zebrafish *in vivo* (factor 1.8 at a depth of 62 μm, factor 1.9 at depth between 71 and 101 μm) could be crucial in many photon-starved experiments, for example, in FLIM-FRET studies where a 2-fold signal improvement can make the difference between a single or double exponential curve fit. The look-up table approach, however, is only valid for relatively homogeneous samples exhibiting dominating depth-specific aberrations that do not fluctuate over short time scales such as, for example, a beating heart. The sample used to create the look-up table needs to be chosen appropriately such that it has a similar average refractive index to that of the sample of interest.

The optimization on a fluorescent dye corrected mainly for system-induced aberrations—that is all aberrations in the optical setup up to the coverslip plus an approximation of the coverslip/water-tissue interface. This approximation was improved by increasing the refractive index of the watery solution with sucrose to a higher refractive index of 1.39, close to that of many biological tissues. The erythrosine solution had the advantages of low cost, ease of preparation, and relative insensitivity to photobleaching due to diffusion of photobleached molecules out of the focal volume. Although the embedding of fluorescent beads is straightforward in organotypic tissue cultures, it is not at all practical in biological tissue. In this regard, aqueous dye can be used with ease for optimization in conjunction with any sample. Using the DMM shape optimized on erythrosine dye, the signal improvement factor up to imaging depths of 60 μm was on average 1.9 ± 0.2 and 1.7 ± 0.2 for depths from $\approx$50 to 110 μm in *ex vivo* mousse tissue.

If the user is able to run optimizations on the same day as the imaging and at an appropriate depth, improvement factors are higher. Using the DMM shape for system aberration correction as an intelligent starting point for optimizations that are depth specific allows for a straightforward method to correct for sample-induced aberrations. The depth specificity of the DMM shapes and analysis of the Zernike aberrations show that a part of the correction was due to the compensation of sample-induced aberrations. Although the best improvements were obtained using SHG from the actual sample to be imaged

with fluorescence, the SHG signal is highly variable in biological tissues. Endogenous SHG is advantageously distributed throughout the sample, does not photobleach and is efficiently generated by type I collagen, which is found in many but not all biological tissues. Although this approach will be very useful for some tissues, for example, such as intestine, every sample may not produce SHG.

It is worthwhile to bear in mind that, even though the development of spherical aberration with imaging depth in a simplified model of a stratified medium is well understood,[44] the correction of spherical aberration by blindly applying a theoretically calculated DMM shape[45] also requires experimental steps. The DMMs are modal correction elements which use a set of smooth functions, the influence functions to approximate the required wavefront. Influence functions correspond to the response of the membrane to the action of every isolated actuator, activated with a known voltage. The influence functions are generally measured with an interferometer and grouped in the influence function matrix. The inverse problem of calculating a set of actuator voltages for the generation of a given wavefront is solved by inverting the influence function matrix to obtain the control matrix. The control matrix of the membrane is the function that translates required surfaces to sets of voltages. Our approach works with every DMM without prior measurements of its influence functions and therefore is especially suitable for life science labs because of its straightforward implementation and practicality of use. Additionally, no prior knowledge of the sample and the aberrations it creates is needed. When the sample that was used to generate the look-up table is also the sample of interest, our approach corrects for the bulk aberration introduced by mismatches in refractive indices and also for sample-induced, field-dependent aberrations.

The search space of mirror shapes is, in theory, of infinite dimensions. However, as the shape of the DMM is controlled via 32 actuators, the search space of possible mirror shapes is in practice reduced to 32 dimensions. Within this search space, there is no certainty that a unique solution exists to a given problem as several different mirror shapes could well lead to the same improvement in merit factor. Inversely, each optimization could end in a different mirror shape if it were to be repeated under the exact same conditions and not left to run indefinitely, giving a possible explanation for the variation of Zernike coefficients with imaging depth observed in Fig. 6. Due to the random nature of the optimization algorithm, a global rather than a local extrema is found if the algorithm is left to run long enough. In this work, an optimization took tens of minutes. The convergence time could be reduced if the optimization algorithm was based on the decomposition of wavefronts into the 15 lowest order Zernike aberrations rather than actuator voltages thereby effectively reducing the search space by half.

It should be noted that the resolution of the optical system was not affected by our optimizations. As can be seen for example in Fig. 4, the full-width-half-maximum of the Gaussian fits remain unchanged. If resolution is of highest importance for the user, the merit factor needs to be chosen such that it reflects the information content of the image, for example sharpness. We also observed a certain amount of axial and lateral shift when comparing image stacks that were acquired with different DMM shapes. The shifts were in the order of $\leq$1 μm and remained linear. The shifts represent a simple geometric distortion and are caused by varying low order aberrations like tip, tilt, and defocus

between various shapes of the DMM. The information content within one stack, however, is not affected.

5 Conclusion

We have demonstrated the use of a DMM in conjunction with a random search algorithm as an AO elements in a nonlinear microscope to improve signal intensity levels at depths in tissues that suffer from photobleaching. All our approaches are aimed at minimizing photon exposure to the sample under investigation. We have investigated preoptimizing the DMM on extrinsic TPEF signal sources like fluorescent dyes and beads, which deliver ample fluorescence signal whose photobleaching is of no consequence to the tissue of interest. In addition, we have optimized on endogenous SHG signal which does not suffer from photobleaching. Thus, the use of bright guide stars that can pollute the fluorescence image and hide small sample features is avoided. The utility of optimizing on SHG is especially pronounced for *in vivo* imaging, where collagen is ubiquitous and samples generally contain enough to run optimizations. In this way, the exposure of fragile fluorescent structures to photons is minimised to imaging.

Our strategies to work around photobleaching in our optimization algorithm are based on a bleaching compensation routine incorporated into the general random search algorithm for use with merit factors liable to photobleaching. We also implemented a Gaussian-weighted selection process in the otherwise random selection of the actuators and used preoptimized DMM shapes from more shallow depths as an intelligent starting point for the optimization at hand. Both approaches speed up the optimization routine and further reduce the effect of photobleaching.

The benefits of wavefront compensation for system- and sample-induced aberrations were demonstrated in organotypic tissue cultures and freshly excised mouse tissue. We investigated the use of look-up tables which are compiled of preoptimized DMM shapes at certain depths. In this way, we demonstrated immediate signal intensity improvement by factors ranging from 1.7 to 4.7. Using look-up tables, signal intensity was increased by a factor of two when imaging zebrafish *in-vivo*. Increasing the signal-to-noise ratio at depth allows for the incident laser power to be reduced, which decreases the risk of photobleaching and improves sample viability.

References

1. W. Denk, J. Strickler, and W. Webb, "Two-photon laser scanning fluorescence microscopy," *Science* **248**(4951), 73–76 (1990).
2. F. Helmchen and F. Denk, "Deep tissue two-photon microscopy," *Nat. Methods* **2**(12), 932–940 (2005).
3. V. Andresen et al., "Infrared multiphoton microscopy: subcellular-resolved deep tissue imaging," *Curr. Opin. Biotech.* **20**(1), 54–62 (2009).
4. H. Jacobsen et al., "Refractive-index-induced aberrations in two-photon confocal fluorescence microscopy," *J. Microsc.* **176**(3), 226–230 (1994).
5. C. de Grauw et al., "Imaging properties in two-photon excitation microscopy and effects of refractive-index mismatch in thick specimens," *Appl. Opt.* **38**(28), 5995–6003 (1999).
6. R. Niesner et al., "The power of single and multibeam two-photon microscopy for high-resolution and high-speed deep tissue and intravital imaging," *Biophys. J.* **93**(7), 2519–2529 (2007).
7. H. Gerritsen and C. De Grauw, "Imaging of optically thick specimen using two-photon excitation microscopy," *Microsc. Res. Tech.* **47**(3), 206–209(1999).
8. H. Babcock, "The possibility of compensating astronomical seeing," *Publ. Astron. Soc. Pac.* **65**(386), 229–236 (1953).
9. J. Girkin, S. Poland, and A. Wright, "Adaptive optics for deeper imaging of biological samples," *Curr. Opin. Biotech.* **20**(1), 106–110 (2009).
10. M. Booth, "Adaptive optics in microscopy," *Philos. T. Roy. Soc. A* **365**(1861), 2829–2843 (2007).
11. M. Neil et al., "Adaptive aberration correction in a two-photon microscope," *J. Microsc.* **200**(2), 105–108 (2000).
12. M. Rueckel, J. Mack-Bucher, and W. Denk, "Adaptive wavefront correction in two-photon microscopy using coherence-gated wavefront sensing," *Proc. Natl. Acad. Sci.* **103**(46), 17137–17142 (2006).
13. J. Cha, J. Ballesta, and P. So, "Shack-hartmann wavefront-sensor-based adaptive optics system for multiphoton microscopy," *J. Biomed. Opt.* **15**(4), 046022 (2010).
14. R. Aviles-Espinosa et al., "Measurement and correction of in vivo sample aberrations employing a nonlinear guide-star in two-photon excited fluorescence microscopy," *Biomed. Opt. Express* **2**(11), 3135–3149 (2011).
15. O. Azucena et al., "Adaptive optics wide-field microscopy using direct wavefront sensing," *Opt. Lett.* **36**(6), 825–827 (2011).
16. X. Tao et al., "Adaptive optics confocal microscopy using direct wavefront sensing," *Opt. Lett.* **36**(7), 1062–1064 (2011).
17. O. Albert et al., "Smart microscope: an adaptive optics learning system for aberration correction in multiphoton confocal microscopy," *Opt. Lett.* **25**(1), 52–54 (2000).
18. L. Sherman et al., "Adaptive correction of depth-induced aberrations in multiphoton scanning microscopy using a deformable mirror," *J. Microsc.* **206**(1), 65–71 (2002).
19. M. Schwertner, M. Booth, and T. Wilson, "Characterizing specimen induced aberrations for high NA adaptive optical microscopy," *Opt. Express* **12**(26), 6540–6552 (2004).
20. P. Villoresi et al., "Optimization of high-order harmonic generation by adaptive control of a sub-10-fs pulse wave front," *Opt. Lett.* **29**(2), 207–209 (2004).
21. N. Ji, D. Milkie, and E. Betzig, "Adaptive optics via pupil segmentation for high-resolution imaging in biological tissues," *Nat. Methods* **7**(2), 141–147 (2009).
22. D. Débarre et al., "Image-based adaptive optics for two-photon microscopy," *Opt. Lett.* **34**(16), 2495–2497 (2009).
23. A. Jesacher et al., "Adaptive harmonic generation microscopy of mammalian embryos," *Opt. Lett.* **34**(20), 3154–3156 (2009).
24. S. Poland, A. Wright, and J. Girkin, "Evaluation of fitness parameters used in an iterative approach to aberration correction in optical sectioning microscopy," *Appl. Opt.* **47**(6), 731–736 (2008).
25. C. Eggeling, A. Volkmer, and C. A. M. Seidel, "Molecular photobleaching kinetics of rhodamine 6g by one- and two-photon induced confocal fluorescence microscopy," *Chem. Phys. Chem.* **6**(5), 791–804 (2005).
26. A. Hopt, "Highly nonlinear photodamage in two-photon fluorescence microscopy," *Biophys. J.* **80**(4), 2029–2036 (2001).
27. P. Timpson et al., "Organotypic collagen I assay: a malleable platform to assess cell behaviour in a 3-dimensional context," *J. Visualized Exp.* **56**, e3089–e3092 (2011).
28. J. Herz et al., "Expanding two-photon intravital microscopy to the infrared by means of optical parametric oscillator," *Biophys. J.* **98**(4), 715–723 (2010).
29. D. Kobat et al., "Deep tissue multiphoton microscopy using longer wavelength excitation," *Opt. Express* **17**(16), 13354–13364 (2009).
30. I. H. Chen et al., "Wavelength dependent damage in biological multiphoton confocal microscopy," *Opt. Quantum Electron.* **34**(12), 1251–1266 (2002).
31. A. Wright et al., "Exploration of the optimisation algorithms used in the implementation of adaptive optics in confocal and multiphoton microscopy," *Microsc. Res. Tech.* **67**(1), 36–44 (2005).

32. M. C. Müllenbroich, N. McAlinden, and A. J. Wright, "Adaptive optics in an optical trapping system for enhanced lateral trap stiffness at depth," *J. Opt.* **15**(7), 075305–075313 (2013).

33. A. Wright et al., "Adaptive optics for enhanced signal in cars microscopy," *Opt. Express* **15**(26), 18209–18219 (2007).

34. M. C. Müllenbroich et al., "Adaptive nonlinear microscopy for whole tissue imaging," *Proc. SPIE* **8588**, 85881X (2013).

35. P. Marsh, D. Burns, and J. Girkin, "Practical implementation of adaptive optics in multiphoton microscopy," *Opt. Express* **11**(10), 1123–1130 (2003).

36. J. Riedl et al., "Lifeact mice for studying f-actin dynamics," *Nat. Methods* **7**(3), 168–169 (2010).

37. J. J. Dirckx, L. C. Kuypers, and W. F. Decraemer, "Refractive index of tissue measured with confocal microscopy," *J. Biomed. Opt.* **10**(4), 044014 (2005).

38. P. J. Keller, "Imaging morphogenesis: technological advances and biological insights," *Science* **340**(6137), 1234168 (2013).

39. J. Bakkers, "Zebrafish as a model to study cardiac development and human cardiac disease," *Cadriovasc. Res.* **91**(2), 279–288 (2011).

40. L. I. Zon, "Zebrafish: a new model for human disease," *Genome Res.* **9**(2), 99–100 (1999).

41. R. Dahm, "The zebrafish exposed see-through mutants may hold the key to unraveling the mysteries of embryonic development," *Am. Sci.* **94**(5), 446–453 (2006).

42. N. Olivier, D. Débarre, and E. Beaurepaire, "Dynamic aberration correction for multiharmonic microscopy," *Opt. Lett.* **34**(20), 3145–3147 (2009).

43. J. Bueno, E. Gualda, and P. Artal, "Adaptive optics multiphoton microscopy to study ex vivo ocular tissues," *J. Biomed. Opt.* **15**(6), 066004 (2010).

44. P. Török et al., "Electromagnetic diffraction of light focused through a planar interface between materials of mismatched refractive indices: an integral representation," *J. Opt. Soc. Am. A* **12**(2), 325–332 (1995).

45. P. Kner et al., "High-resolution wide-field microscopy with adaptive optics for spherical aberration correction and motionless focusing," *J. Microsc.* **237**(2), 136–147 (2010).

Marie Caroline Müllenbroich received a German Diplom and a MSc from the University of Heidelberg in 2008. She then completed her PhD at the Institute of Photonics at the University of Strathclyde, Glasgow in the field of Adaptive Optics and Microscopy in 2012. She is currently a postdoc at the European Laboratory for Nonlinear Spectroscopy (LENS) at the University of Florence where she is working on light sheet microscopy as part of the Human Brain Project.

Ewan J. McGhee has been interested in applying his experience in high resolution microscopy and spectroscopy to many interesting challenges in biology since being a postdoctoral researcher in the Photonics group at Imperial College London in 2009. Since then he has been a researcher at the Beatson Institute for Cancer Research Glasgow where he works on applying new techniques to high resolution in vivo microscopy.

Amanda J. Wright studied for her undergraduate and postgraduate degrees at the University of Manchester before moving to the Institute of Photonics, University of Strathclyde, initially as research associate and then associate team leader. In 2007, she was awarded a Royal Academy of Engineering / EPSRC research fellowship which she transferred to the University of Nottingham in 2012, becoming a member of academic staff and part of IBIOS (Institute for Biophysics, Imaging and Optical Science).

Kurt I. Anderson completed his PhD at the University of Salzburg in 1997 then spent 2 years at the Marie Curie Cancer Research Institute (UK) before moving to Dresden in 2001 to set up the light microscopy facility at the new MPI-CBG. In 2005 he moved to the Beatson Institute for Cancer Research, where he runs the Beatson Advanced Imaging Resource (BAIR) and a research group using advanced imaging methods to investigate tumor cell migration.

Keith Mathieson is director of the Institute of Photonics at the University of Strathclyde and leads the Neurophotonics research group. He gained a PhD in physics (2001) from the University of Glasgow and in 2005 was awarded a Royal Society of Edinburgh Fellowship. He moved on to a research position at UC Santa Cruz and won an RCUK Fellowship (SU2P) to Stanford University. There he helped develop an optoelectronic retinal prosthesis and studied retinal processing.